

Protection of pyrolysis gases combustion against charring materials' surface ablation

Weijie LI¹, Haiming HUANG^{1*}, Qing WANG², Zimao ZHANG¹

¹Institute of Engineering Mechanics, Beijing Jiaotong University, Beijing, 100044, China

²School of Engineering and Computing Sciences, Durham University, Durham, DH1 3LE, UK.

* Corresponding author: huanghaiming@tsinghua.org.cn

Abstract

Charring ablation materials are widely used for thermal protection systems in a vehicle during hypersonic reentry. The pyrolysis gases from the charring materials can react with oxygen in the boundary layer, which makes the surface ablation rate decrease. The problem of protection of combustion of pyrolysis gases in charring material against surface ablation is solved by the detached normal shock wave relations and the counterflow diffusion flame model. The central difference format for the diffusion term and the upwind scheme for the convection term are used to discretize the mathematical model of the counterflow diffusion flame. Numerical results indicate that the combustion of pyrolysis gases in the boundary layer can completely protect the material surface from recession when the velocity of pyrolysis gases injecting to the boundary layer is higher than the critical velocity. There is an allometric relationship between the critical velocity and Mach number, and the combustion heat has little influence on the temperature distribution originating from the aerodynamic heating. This study will be helpful for the design of the thermal protection system in hypersonic reentry vehicles.

Keywords: Charring materials, Pyrolysis gases, Counterflow diffusion flame, Surface ablation, Critical velocity.

1. Introduction

Charring ablation material is the first choice for the thermal protection system of a vehicle subjected to severe aerodynamic environment during hypersonic reentry [1-3]. The pyrolysis of charring ablation materials and the flow of pyrolysis gases in the material can bring off amounts of heat [4-7]. Meanwhile, the char on the material surface usually ablates because it reacts with the oxygen in the boundary layer behind the shock wave. Based on the thermal protection mechanism of charring materials, researchers developed three types of physical and mathematical models for the materials [5, 8-13]. A heat conduction equation combining with the Arrhenius law was widely used to estimate the pyrolysis of a charring material avoiding seeking moving interfaces in the material. The other two models - the pyrolysis interface model and the pyrolysis layer model - were built well, reflecting the materials' multilayer phenomenon. Regrettably, there are still deficiencies in the three types of models above, especially the surface ablation rate considered in them as a function of surface temperature without pyrolysis gases reacting with oxygen. Actually, this surface ablation rate depends not only on the surface temperature, but also on the combustion of pyrolysis gases.

When pyrolysis gases injected from the inner material meet the oxygen, a diffusion flame is formed. A starting reaction interface between pyrolysis gases and oxygen is defined as the position where the mole fraction of oxygen just shifts from a positive value to zero. If the starting reaction interface reaches or enters the material surface, char on the surface could react with the oxygen. In this case, combustion of pyrolysis gases partly protects the material surface. If the starting reaction interface stays outside the material surface, char on the surface cannot react with the oxygen. As a result, combustion of pyrolysis gases completely protects the material from surface ablation. Notably, the velocity of pyrolysis gases when the starting reaction interface just reaches the material surface is significant. We can call this velocity the 'critical velocity'. Up to now, research on the protection of combustion of pyrolysis gases from charring materials remains a longstanding challenge because of lack of references to this problem.

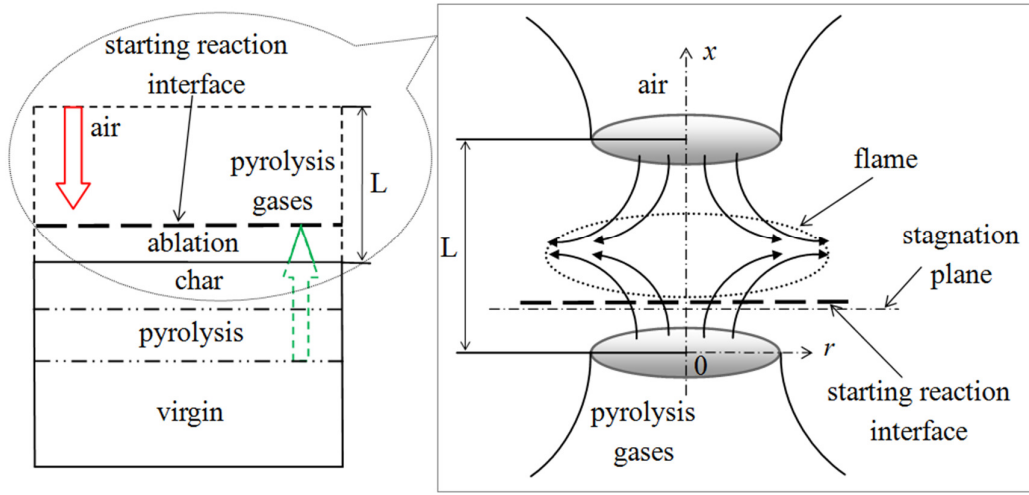
The counterflow diffusion flame model, describing a fundamental combustion configuration, can be applied for solving combustion problems [14-18]. The mathematical model of the heat and mass transport processes must take numbers of chemical reactions, gas-phase multi-component viscosities, thermal conductivities, diffusion coefficients, thermal diffusion coefficients, thermodynamics and chemical rates into consideration [19-31]. However, the combination of counterflow diffusion flame and surface ablation of charring materials has never been reported. In this paper, the problem of the protection of pyrolysis gases combustion against charring materials' surface ablation is solved by numerical methods on the basis of the counterflow diffusion flame.

2. Models

2.1. Physical model

With charring material of a vehicle subject to severe aerodynamic environment, the heat transfers to the inner material and the temperature of the material increases from the material surface to the bondline. When the temperature at the surface reaches the temperature of commencing pyrolysis for phenolic resin, the material starts appearing in layers, namely, a virgin layer and a pyrolysis layer. Meanwhile, the pyrolysis gases generated from the material in the pyrolysis layer flow to the material surface and inject to the boundary layer adjacent to the material surface. Heating continues and the surface temperature reaches the temperature of completing pyrolysis for phenolic resin. Three layers: the virgin layer, the pyrolysis layer and the char layer, are produced in the material. In the range of the high temperature and high pressure boundary, the pyrolysis gases, which are usually hydrogen, methane, carbon monoxide, carbon dioxide, water and ethane, can be burnt with the oxygen in the boundary layer.

A counterflow diffusion flame model can describe the combustion phenomena of pyrolysis gases in the boundary layer. In the counterflow diffusion flame model, the material surface can be seen as the fuel nozzle, the detached normal shock wave can be seen as the oxidizer nozzle, and the region of the boundary layer can be seen as the range of diffusion combustion. Fig. 1 illustrates a schematic of a counterflow diffusion flame representing the pyrolysis gases reacting with the oxygen in the boundary layer adjacent to the material surface.



(a) One-dimensional ablation model (b) Pyrolysis gases-air counterflow diffusion flame

Fig. 1. Schematic diagram of combustion of pyrolysis gases from charring material in the boundary layer

In Fig. 1(a), a one-dimensional ablation model of charring material is presented. With the increasing temperature of the inner material, the pyrolysis gases generate flow through the inner material and inject to the boundary layer, whose thickness is L . The oxygen flows from the detached normal shock wave toward the material surface. The bold dashed line in Fig.1 represents the starting reaction interface.

The pyrolysis gases-air counterflow diffusion flame in Fig. 1(b) describes the combustion phenomena in the boundary layer in detail. If we let x and r denote the independent spatial coordinates in the axial and the radial directions, respectively, the material surface is located at $x=0$ and the detached normal shock wave is located at $x=L$. At $x=0$, the pyrolysis gases flow toward the positive x direction. At $x=L$, the oxygen flows toward the negative x direction. The stagnation plane is the position where the velocity of gases is zero.

2.2. Mathematical models

Based on the physical model, the mathematical model for the phenomena of pyrolysis gases combustion in the boundary layer can be considered as two parts, as follows.

2.2.1. Detached normal shock wave relations

To obtain one of the boundary conditions in the counterflow diffusion flame, the temperature, pressure, gas density and gas velocity behind the detached normal shock wave, which are seen as the boundary conditions, should be calculated first. The mass conservation equation, the momentum conservation equation and the energy conservation equation of the detached normal shock wave can be written as

$$\rho_f u_f = \rho_b u_b \quad (1)$$

$$p_f + \rho_f u_f^2 = p_b + \rho_b u_b^2 \quad (2)$$

$$h_f + \frac{u_f^2}{2} = h_b + \frac{u_b^2}{2} \quad (3)$$

where ρ , u , p and h are the density, velocity, pressure and specific enthalpy of gas, respectively. And the subscript f and b , respectively, represent the position before and after the detached normal shock wave.

The thermodynamic properties of air with real gas effects may be denoted by [32]

$$h = h(p, \rho) \quad (4)$$

$$T = T(p, \rho) \quad (5)$$

The specific enthalpy, pressure, gas density and gas velocity behind the detached normal shock wave can be obtained from Eqs. (1)-(4). Then the temperature can be expressed by eq. (5). These results can be seen as the boundary conditions at the oxidizer nozzle in the counterflow diffusion flame.

2.2.2. Counterflow diffusion flame solutions

The calculation of the critical velocity $u_{s,c}$ of pyrolysis gases at the material surface is significant in the problem. A counterflow diffusion flame is applied to solve the critical velocity, temperature and main components' mole fraction in the problem. The simplifying assumptions of the counterflow diffusion flame are as follows: (a) the temperature and species mass fractions are functions of x alone; (b) the thermodynamic pressure is constant throughout the flow field in the axial direction, but the pressure gradient term appears in the momentum equation in the radial direction [23]. Based on the Navier-Stokes equations in cylindrical coordinates, the physiochemical processes are expressed by the following conservation equations in the axisymmetric system [23, 24]

$$G - \frac{dF}{dx} = 0 \quad (6)$$

$$\frac{d}{dx} \left[\mu \frac{d}{dx} \left(\frac{G}{\rho} \right) \right] - 2 \frac{d}{dx} \left(\frac{FG}{\rho} \right) + \frac{3}{\rho} G^2 + H = 0 \quad (7)$$

$$2Fc_p \frac{dT}{dx} - \frac{d}{dx} \left(\lambda \frac{dT}{dx} \right) + \sum_k \rho c_{pk} Y_k V_k \frac{dT}{dx} - \sum_k h_k \omega_k W_k = 0 \quad (8)$$

$$2F \frac{dY_k}{dx} + \frac{d}{dx} (\rho Y_k V_k) - \omega_k W_k = 0 \quad (9)$$

$k = 1, 2, \dots, K$

where $G(x) = -\frac{\rho v}{r}$, $F(x) = \frac{\rho u}{2}$.

In these equations, u and v are respectively the axial and radial velocity, μ is the dynamic viscosity which is detailed in ref. [31], λ is the thermal conductivity, Y is the mass fraction, V is the diffusion velocity, h is the enthalpy, ω is the chemical reaction rate and W is the molecular weight. The subscript k is the species index. In addition, H is the eigenvalue for the radial

pressure gradient which is equal to the pressure at the position behind the detached normal shock wave

$$H = \frac{1}{r} \frac{\partial p_b}{\partial r} \equiv \text{constant} \quad (10)$$

The parameters c_p and λ in eqs. (6)-(9) are respectively given as

$$c_p = \sum_{k=1}^K c_{pk} Y_k = \sum_{k=1}^K \frac{C_{pk}}{W_k} Y_k \quad (11)$$

$$\lambda = \frac{1}{2} \sum_{k=1}^K X_k \lambda_k + \frac{1}{\sum_{k=1}^K X_k / \lambda_k} \quad (12)$$

where the mean molecular weight $\bar{W} = \frac{1}{\sum_{k=1}^K Y_k / W_k}$, C_{pk} is the molar heat capacity at constant

pressure of k th species, and X_k is the mole fraction of the k th species expressed as $X_k = \frac{Y_k \bar{W}}{W_k}$.

The diffusion velocity can be expressed as

$$V_k = -\frac{1}{X_k} D_{km} \frac{dX_k}{dx} - \frac{D_k^T}{\rho Y_k} \frac{1}{T} \frac{dT}{dx} \quad (13)$$

where $D_{km} = \frac{1 - Y_k}{\sum_{j \neq k} X_j / D_{jk}}$ and D_{jk} , D_{km} , D_k^T are multi-component, mixture averaged and

thermal diffusion coefficients, respectively, which are shown in detail in ref. [33].

The chemical reaction rate is a complicated parameter written as [31]

$$\omega_k = \sum_{i=1}^I (v_{ki}^* - v_{ki}^{\prime}) [k_{fi} \prod_{k=1}^K [X_k]^{v_{ki}^{\prime}} - k_{ri} \prod_{k=1}^K [X_k]^{v_{ki}^*}] \quad (14)$$

where v_{ki}^{\prime} and v_{ki}^* are the stoichiometric coefficients of the k th reactant and product species in the i th reaction, k_{fi} and k_{ri} are respectively the forward and the reverse rate constant of the i th

reaction, and the molar concentration of the k th species $[X_k] = \rho \frac{Y_k}{W_k}$.

The boundary conditions for the pyrolysis gases and air streams at the material surface (s) and the position behind the detached normal shock wave (b) are

$$x = 0: F = \rho_s u_s / 2, \quad G = 0, \quad T = T_s, \quad \rho u Y_k + \rho Y_k V_k = (\rho u Y_k)_s \quad (15)$$

$$x = L: F = \rho_b u_b / 2, \quad G = 0, \quad T = T_b, \quad \rho u Y_k + \rho Y_k V_k = (\rho u Y_k)_b \quad (16)$$

The boundary conditions above specify the total mass flux, including diffusion and convection, rather than the species fraction ($Y_k = Y_{k,s}$). If gradients exist at the boundary, these conditions

allow diffusion into the nozzle.

In addition, the thickness of the boundary layer, which is the distance of the detached normal shock wave, can be expressed as [34]

$$L = s\rho_f / (\rho_f + \rho_b) \quad (17)$$

where s is the curvature radius at the stagnation point for a re-entry vehicle.

The counterflow diffusion flame is seen as a two-point boundary value problem for the dependent variables (F, G, T, Y_k, H), which can be solved by the differential eqs. (6)-(10) and the boundary conditions.

3. Numerical methods

The nonlinear mathematical model in Section 2.2.1 can be solved by the Quasi-Newton methods with our FORTRAN codes. And the mathematical model for the counterflow diffusion flame is regarded as large-scale nonlinear equations. To obtain the temperatures and mole fractions of the main component distributions of the counterflow diffusion flame, it is necessary to discretize the differential equations. We adopt the central difference format for the diffusion term and the upwind scheme for the convection term. Final discrete formats of eqs. (6)-(9) can be expressed as follows

$$-\frac{F_j - F_{j-1}}{\Delta x} + G_j = 0 \quad (18)$$

$$\begin{aligned} \frac{1}{\Delta x^2} [(\mu_j - \mu_{j-1}) \left(\frac{G_j}{\rho_j} - \frac{G_{j-1}}{\rho_{j-1}} \right) + \mu_j \left(\frac{G_{j+1}}{\rho_{j+1}} - 2 \frac{G_j}{\rho_j} + \frac{G_{j-1}}{\rho_{j-1}} \right)] \\ - \frac{2}{\Delta x} \left(\frac{F_j G_j}{\rho_j} - \frac{F_{j-1} G_{j-1}}{\rho_{j-1}} \right) + \frac{3}{\rho_j} G_j^2 + H_j = 0 \end{aligned} \quad (19)$$

$$\begin{aligned} -\frac{1}{\Delta x^2} [(\lambda_j - \lambda_{j-1})(T_j - T_{j-1}) + \lambda_j(T_{j+1} - 2T_j + T_{j-1})] \\ + \frac{T_j - T_{j-1}}{\Delta x} (2F_j c_{p,j} + \sum_k \rho_j c_{pk,j} Y_{k,j} V_{k,j}) - \sum_k h_{k,j} \omega_{k,j} W_{k,j} = 0 \end{aligned} \quad (20)$$

$$\begin{aligned} \frac{1}{\Delta x} [2F_j (Y_{k,j} - Y_{k,j-1}) + (\rho_j Y_{k,j} V_{k,j} - \rho_{j-1} Y_{k,j-1} V_{k,j-1})] - \omega_{k,j} W_{k,j} = 0 \\ k = 1, 2, \dots, K \end{aligned} \quad (21)$$

where subscript j represents the space point in the x direction from the material surface to the position behind the detached normal shock wave.

4. Numerical results

Suppose that a vehicle whose curvature radius at the stagnation point is 4.694m re-enters from an altitude of 55km at hypersonic speed ($Ma=5, 6, 7, 8, 9$ and 10 respectively for the examples), and the gases' temperature (T_s) of the material surface is 1400K at this altitude. The flow conditions of the atmosphere at altitude 55km are given in Table 1.

Table 1 The flow condition of atmosphere at altitude 55km

T_f [K]	p_f [Pa]	ρ_f [kg/m ³]	a [m/s]
265.59	42.752	0.00056075	326.7

where a is the speed of sound at altitude 55km.

4.1. Temperature, pressure, gas density and gas velocity behind the detached normal shock wave

In order to obtain the boundary conditions at $x=L$ in the counterflow diffusion flame, the relationships in Section 2.2.1 and the expression for L in Section 2.2.2 are used to calculate T_b , p_b , ρ_b , u_b and L , which are shown in Table 2.

Table 2 The fluid parameters behind the detached normal shock wave

Ma	u_b [m/s]	ρ_b [kg/m ³]	p_b [Pa]	T_b [K]	L [m]
5	298.610	0.003067	1265.5	1429.459	0.725563
6	322.756	0.003406	1842.6	1862.781	0.663556
7	335.861	0.003818	2544.7	2269.798	0.601121
8	334.349	0.004383	3383.2	2579.057	0.532422
9	330.877	0.004983	4345.1	2822.788	0.474798
10	330.627	0.005541	5422.1	3074.322	0.431378

It can be seen in Table 2 that with an increasing Ma , the density, pressure and temperature behind the detached normal shock wave respectively gets higher, however, the boundary thickness gets lower, and the velocity behind the detached normal shock wave changes a little.

Using the results shown in Table 2 as the boundary conditions for each Ma , giving different velocities of pyrolysis gases at the material surface, the temperature and mole fraction distributions in the counterflow diffusion flame can be calculated.

4.2. Temperature and mole fraction distributions in the counterflow diffusion flame when $u_s=50m/s$

The hydrocarbons are produced as pyrolysis gases during the pyrolysis of a charring ablation material. These hydrocarbons flow to the material surface and inject to the boundary layer. Table 3 gives the mole fractions of the main components of the pyrolysis gases which can be seen as the boundary conditions at $x=0$ for each Ma [35]. Together with the results in Table 2 as the boundary conditions for air, which includes O_2 (21% mass fraction) and N_2 (79% mass fraction) at $x=L$, Eqs. (18)-(21) are taken into consideration to obtain the temperature and mole fractions of main components in the pyrolysis gases-air diffusion flame when $u_s=50m/s$. It is necessary to pay attention to the fact that the reactions between the components of Table 3 and the oxygen in the boundary layer can be shown by the detailed mechanisms from GRI-Mech 3.0 [36]. The straight, dash, dot, dash-dot, dash-dot-dot and short dash lines represent the result curves for $Ma=5, 6, 7, 8, 9$ and 10 , respectively, in Figs. 2-4.

Table 3 The components' mole fractions of the pyrolysis gases at the material surface [35]

H_2	CH_4	CO	H_2O	CO_2	C_2H_6
59.4%	14.9%	12.7%	12.7%	0.2%	0.1%

Fig. 2 shows the comparisons between the temperature distributions for different Ma . It can be seen that the temperature distribution presents as a convex parabola curve for $Ma=5, 6$ or 7 . The region corresponding to the temperature change is the reaction zone of the pyrolysis gases and air. With an increasing Ma , the temperature at the position behind the detached normal shock wave increases and exceeds the beginning reaction temperature of the pyrolysis gases and air. Furthermore, the convex parabola curve cannot be seen in the temperature distribution. The phenomena tell us that the combustion heat has little influence on the temperature distribution, which comes from the aerodynamic heating. And the influence becomes weaker with an increasing Ma . In the enlarged picture, the combustion reaction zone of the pyrolysis gas is specified between the two vertical lines. It also can be seen that with increasing Mach number, this zone becomes narrower.

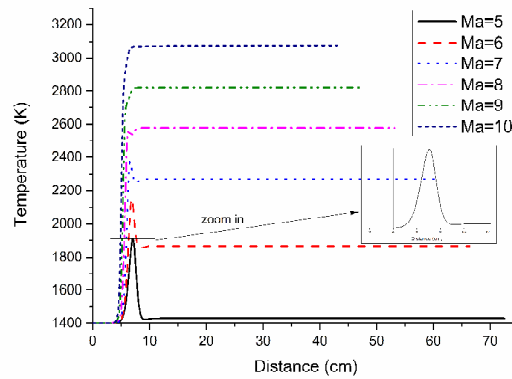


Fig. 2. Comparisons between the temperature distributions for different Ma

In Figs. 3(a)-3(g), the mole fractions of H_2 , CH_4 , CO , H_2O , CO_2 , C_2H_6 and O_2 from combustion in the boundary layer for different Ma are displayed. In Fig. 3(a), it can be seen that the mole fraction curve of H_2 is monotonic in the reaction zone. It demonstrates that the consumption amount is more than that of the production amount for H_2 in combustion. Moreover, with an increasing Ma , the reaction region becomes narrower and the consumption rate for H_2 increases. In Figs. 3(b)-3(e), the mole fraction curves of CH_4 , CO , H_2O and CO_2 are each a convex parabola in the reaction region. It is clear that the production amounts exceed the consumption amounts for above four components in the pyrolysis gases-air diffusion flame in the boundary layer. With an increasing Ma , the production amounts of CH_4 decrease, however, the production amount of CO increases. The production amount of H_2O increases when the Mach number increases from 5 to 7, and it decreases when the Mach number increases from 7 to 10. The production amount of CO_2 increases when the Mach number increases from 5 to 8, and it decreases when the Mach number increases from 8 to 10. In Fig. 3(f), C_2H_6 decreases when it just comes out of the material surface as consumption. In the reaction region, it functions as production and increases. And with an increasing Mach number, the amount of C_2H_6 decreases. In Fig. 3(g), the starting reaction interface moves further away from the material surface with an increasing Ma .

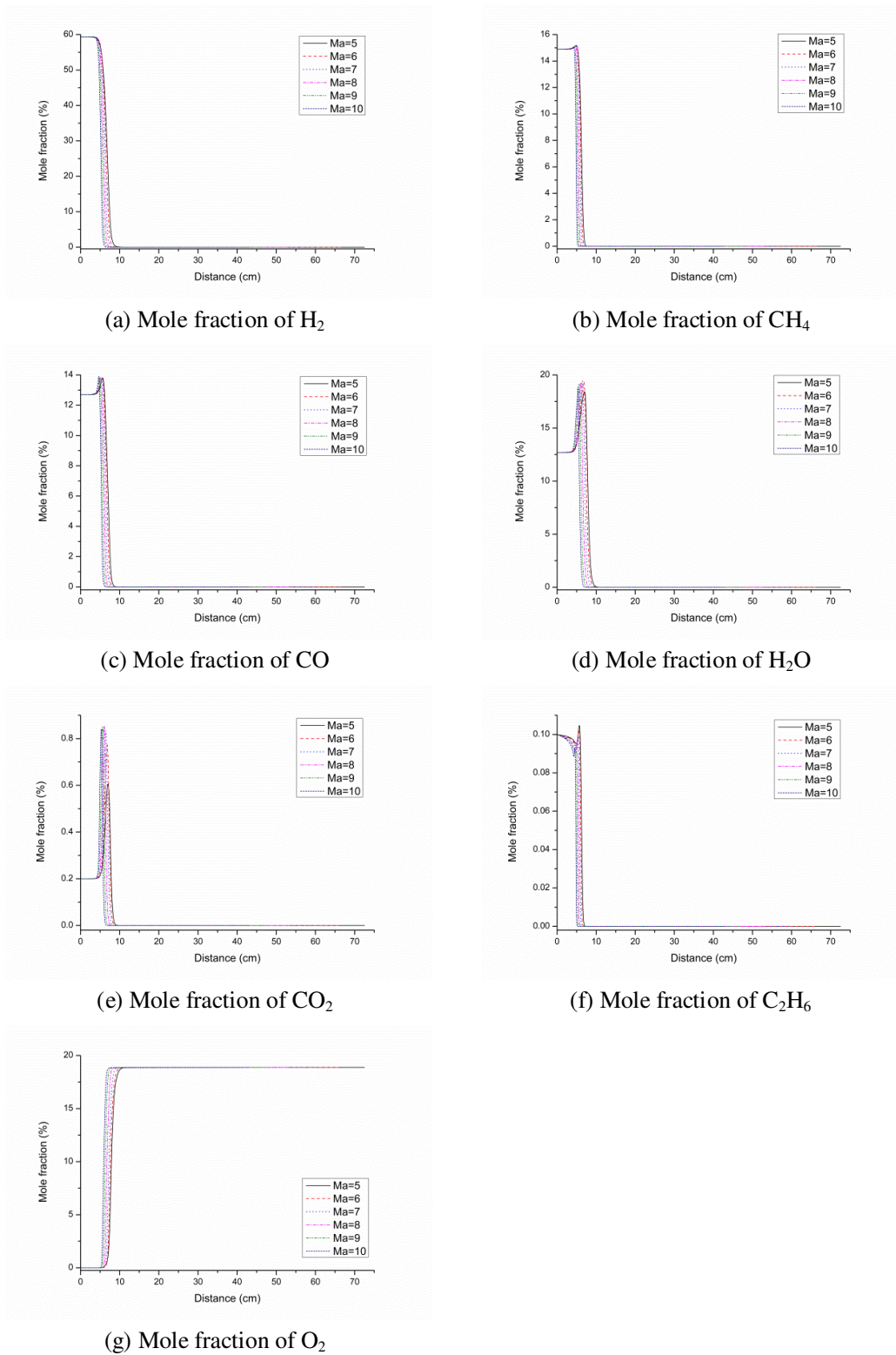


Fig. 3. Mole fractions of main components from combustion in the boundary layer for different Ma

4.3. Analysis of the critical velocity of pyrolysis gases at the material surface

To find the law of the complete protection by combustion of pyrolysis gases in the boundary layer on charring the ablation materials' surface, it is necessary to know the critical velocity of pyrolysis gases at the material surface. From the boundary conditions in Section 4.2 for each Ma , the mole fraction distribution of O_2 can be obtained by using different gases' velocity at the material surface. In these O_2 mole fraction results, it is discovered that when the case in which the starting reaction interface just reaches the material surface, the critical velocity of pyrolysis gases at the material surface for each Ma is obtained. Table 4 gives the critical velocity result for each Ma .

Table 4 The critical velocity of pyrolysis gases at the material surface for different Ma

Ma	5	6	7	8	9	10
$u_{s,c}$ [m/s]	11.00	6.00	3.50	2.17	1.57	1.20

Fig. 4 shows the comparison between the types of main components at the starting reaction interface when $u_s = u_{s,c}$ for each Ma . The main components include H_2 , H_2O , N_2 , CH_4 and CO for $Ma=5$; H_2 , H , H_2O , N_2 , CH_3 , CH_4 and CO for $Ma=6$; H_2 , H , H_2O , N_2 , CH_3 , CH_4 , CO and CO_2 for $Ma=7$, H_2 , H , H_2O , N_2 , CH_3 , CH_4 , CO , CO_2 and C_2H_2 for $Ma=8, 9$ and 10 . It is visible that with an increasing Ma , the types of combustion components increase, the consumption rate of H_2 increases, the production amounts of CH_3 increases at first then decreases, the production amount of CH_4 decreases, the production amount of CO has little difference and the production amounts of H , CO_2 , C_2H_2 and H_2O increase.

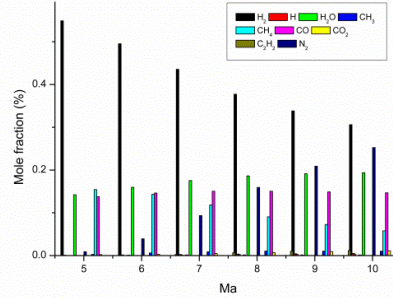


Fig. 4. Comparison of the types of main components at the starting reaction interface

Fig. 5 shows the relationship between the critical velocity of pyrolysis gases and Mach number (at 55km). Every square dot represents the calculated critical velocity of pyrolysis gases at the material surface for each Mach number. The curve fitting results of these data are shown by the smooth curve. The results show that the injection velocity of pyrolysis gases at the material surface, which can lead to the starting reaction interface just reaching the material surface, decreases gradually with an increasing Mach number. Furthermore, by analyzing the fitted curve, an allometric function relationship between the critical velocity of pyrolysis gases at the material surface and the Mach number is identified. At the altitude of 55km, this function can be written as

$$u_{s,c} = 2000.78Ma^{-3.25} \quad (22)$$

To validate the accuracy of eq. (27), another calculation establishes the critical velocity of pyrolysis gases at the material surface for $Ma=5.5, 6.5, 7.5, 8.5$ and 9.5 . The round dots in Fig. 5 describe the critical velocities for $Ma=5.5, 6.5, 7.5, 8.5$ and 9.5 . The round dots are in agreement with the fitted curve. It can be concluded that the allometric function can describe the relationship between the critical velocity of pyrolysis gases at the material surface and Mach number at an altitude of 55km.

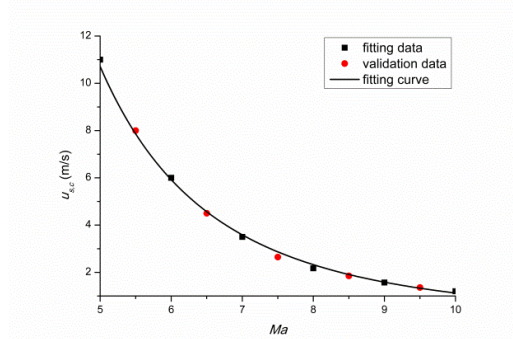


Fig. 5. The critical velocities of pyrolysis gases at the material surface and Mach numbers

Another study of the relationship between the critical velocity of pyrolysis gases at the material surface and the Mach number is developed when the altitude changes. The purpose of this study is to find whether the allometric function is applicable to the relationship between the critical velocity of pyrolysis gases at the material surface and the Mach number at various altitudes. Table 5 shows the functions for the relationships between the critical velocities and Ma at the altitudes of 40-70km.

Table 5 The functions for the relationships between the critical velocities and Ma at various altitudes

Altitude [km]	$u_{s,c}(Ma)$ [m/s]
40	$u_{s,c} = 7.39Ma^{-1.61}$
44	$u_{s,c} = 21.18Ma^{-1.89}$
50	$u_{s,c} = 276.47Ma^{-2.72}$
55	$u_{s,c} = 2000.78Ma^{-3.25}$
60	$u_{s,c} = 1753.19Ma^{-2.74}$
65	$u_{s,c} = 854.66Ma^{-1.99}$
70	$u_{s,c} = 1441.67Ma^{-1.92}$

The results in Table 5 show that the relationship between the critical velocity of pyrolysis

gases at the material surface and Mach number at every altitude can be calculated with an allometric function, which can be written in a general formula

$$u_{s,c} = A \times Ma^B \quad (23)$$

With the altitude increasing, A in eq. (23) increases from 40km to 55km and then decreases, except the case for the altitude at 65km. And B in eq. (23) decreases from 40km to 55km and then increases. In spite of the formula for each altitude having different coefficients, the allometric function can conclude the relationship between the critical velocity of pyrolysis gases at the material surface and Mach number.

If the injection velocity of pyrolysis gases at the material surface is more than the critical velocity, the starting reaction interface should not reach the material surface. In other words, the combustion of pyrolysis gases in the boundary layer can completely protect the material surface from surface ablation in this situation. The combustion of produced hydrocarbons from material pyrolysis in the boundary layer can completely protect the char on the material surface without surface ablation.

5. Conclusions

This paper focuses on the protection of pyrolysis gases combustion against the surface ablation of charring material in a hypersonic vehicle. By analyzing the temperature, components of combustion, critical velocity of pyrolysis gases at the material surface and the position of the starting reaction interface, the results show that

- (1) The critical velocity of pyrolysis gases at the material surface is important to the surface ablation of charring materials. If the velocity of pyrolysis gases injecting to the boundary layer is higher than the critical velocity, surface ablation would not happen. Otherwise, the combustion of pyrolysis gases in the boundary layer only partly protects the char on the material surface.
- (2) The relationship between the critical velocity of pyrolysis gases at the material surface and Mach number obeys an allometric function. At a fixed altitude of a vehicle hypersonic re-entry, the critical velocity of pyrolysis gases at the material surface, which can lead the starting reaction interface to just reach the material surface, satisfies an allometric function with the Mach number. The critical velocity decreases with an increasing Mach number.
- (3) The heat from the combustion of pyrolysis gases in the boundary layer has little influence on the temperature distribution produced from the aerodynamic heat. With an increasing Mach number, the influence on the temperature distribution becomes weaker.

Acknowledgments

This work was supported by the National Natural Science Foundation of China (11472037 and 11272042).

Nomenclature

L – thickness of boundary layer [m]	u – gas velocity / gas velocity in axial direction [m/s]
x – spatial coordinate in axial direction [m]	p – gas pressure [Pa]
r – spatial coordinate in radial direction [m]	h – specific enthalpy [J/kg]
ρ – gas density [kg/m ³]	

T – gas temperature [K]	D_k^T – thermal diffusion coefficients
c_p – specific heat at constant pressure [J·kg ⁻¹ ·K ⁻¹]	[kg·m ⁻¹ ·s ⁻¹]
G – function of density, radial velocity and radial coordinate [kg·m ⁻³ ·s ⁻¹]	v' – stoichiometric coefficient of reactant [-]
F – function of density and axial velocity [kg·m ⁻² ·s ⁻¹]	v'' – stoichiometric coefficient of product [-]
μ – dynamic viscosity [kg·m ⁻¹ ·s ⁻¹]	s – curvature radius at stagnation point [m]
v – gas velocity in radial direction [m/s]	\dot{m} – mass injection rate [kg·m ⁻² ·s ⁻¹]
λ – thermal conductivity [W·m ⁻¹ ·K ⁻¹]	Ma – Mach number [-]
Y – mass fraction [-]	a – speed of sound [m/s]
V – diffusion velocity [m/s]	
ω – chemical reaction rate [mol·m ⁻³ ·s ⁻¹]	<i>Subscripts</i>
W – molecular weight [kg/mol]	s – surface
\bar{W} – mean molecular weight [kg/mol]	c – critical
C_p – molar heat capacity at constant pressure [J·mol ⁻¹ ·K ⁻¹]	f – the position before detached normal shock wave
X – mole fraction [-]	b – the position behind detached normal shock wave
$[X]$ – molar concentration [mol/m ³]	k – species index
D_{jk} – multicomponent diffusion coefficients [m ² /s]	i – i th reaction
D_{km} – mixture averaged diffusion coefficients [m ² /s]	g – pyrolysis gases
	j – space point in x direction

References

- [1] Y.K. Chen, F.S. Milos, Effects of nonequilibrium chemistry and darcy-forchheimer pyrolysis flow for charring ablator, *J. Spacecraft Rockets* 50(2) (2013) 256-269.
- [2] G.H. Bai S.H. Meng, Prediction on carbon/carbon composites ablative performance by artificial neutral net, *J. Mater. Sci. Technol.* 24(6) (2008) 945-952.
- [3] M. Natali, I. Puri, M. Rallini, Ablation modeling of state of the art EPDM based elastomeric heat shielding materials for solid rocket motors, DOI: 10. 1016/j. commatsci. 2015. 09. 050.
- [4] H. Weng, A. Martin, Multidimensional modeling of pyrolysis gas transport inside charring ablative materials, *J. Thermophys. Heat Tr.* 28(4) (2014) 583-597.
- [5] W.J. Li, H.M. Huang, T. Ye, Nonlinear analysis on thermal behavior of charring materials with surface ablation, *Int. J. Heat Mass Tran.* 84 (2015) 245-252.
- [6] W.J. Li, H.M. Huang, X.L. Xu, Nonlinear pyrolysis layer model for thermal behavior of nonhomogeneous charring materials, *J. Appl. Polym. Sci.* 132 (31) (2015) 42331 .
- [7] C. Yan, R. Liu, Y. Cao, Ablation behavior and mechanism of C/ZrC, C/ZrC-SiC and C/SiC composites fabricated by polymer infiltration and pyrolysis process, *Corros. Sci.* 86(9) (2014) 131-141.
- [8] A.P. Mouritz, S. Feih, E. Kandare, Review of fire structural modelling of polymer composites, *Compos. Part A-Appl.* S.40(12) (2009) 1800-1814.

- [9] B.Y. Lattimer, J. Ouellette, Properties of composite materials for thermal analysis involving fires, *Compos.Part A-Appl. S.37(7)* (2006) 1068-1081.
- [10] B. Yu, N.L. Post, J.J. Lesko, Experimental investigations on temperature-dependent thermo-physical and mechanical properties of pultruded GFRP composites, *Thermochim. ACTA* 469(1-2) (2008) 28–35.
- [11] A. Viviani, G. Pezzella, S. Borrelli, Effect of finite rate chemical models on the aerothermodynamics of reentry capsules, in: 15th AIAA international space planes and hypersonic systems and technologies conference, Dayton, Ohio, 2008, AIAA 2008-2668.
- [12] W.J. Li, H.M. Huang, T. Ye, A nonlinear pyrolysis layer model for analyzing thermal behavior of charring ablator, *Int. J. Therm. Sci.* 98 (2015) 104–112.
- [13] W.J. Li, H.M. Huang, X.L. Xu, Effects of gradient density on effective heat capacity of charring ablative material for re-entry vehicles, *Int. J. Numer. Method H.* 25 (2015) 472-483.
- [14] E.A. Karatas, M. Commodo, Ömer L. Gülder, Soot formation in co- and counter-flow laminar diffusion flames of binary mixtures of ethylene and butane isomers and synergistic effects, *Energ. Fuel.* 24(9) (2010) 4912-4918.
- [15] U. Niemann, K. Seshadri, F.A. Williams, Effect of pressure on structure and extinction of near-limit hydrogen counterflow diffusion flames, *P. Combust. Inst.* 34(1) (2013) 881–886.
- [16] S. Chen, C. Zheng, Counterflow diffusion flame of hydrogen-enriched biogas under MILD oxy-fuel condition, *Int. J. Hydrogen Energ.* 36(23) (2011) 15403-15413.
- [17] B.C. Choi, S.K. Choi, S.H. Chung, Soot formation characteristics of gasoline surrogate fuels in counterflow diffusion flames, *P. Combust. Inst.* 33(1) (2011) 609–616.
- [18] W. Sun, M. Uddi, T. Ombrello, Effects of non-equilibrium plasma discharge on counterflow diffusion flame extinction, *P. Combust. Inst.* 33(6) (2011) 3211–3218.
- [19] G. Dixon-Lewis, T. David, P.H. Gaskell, Calculation of the structure and extinction limit of a methane-air counterflow diffusion flame in the forward stagnation region of a porous cylinder, *Symp. Combust.* 20(1) (1985) 1893–1904.
- [20] H. Tsuji, I. Yamaoka, The structure of counterflow diffusion flames in the forward stagnation region of a porous cylinder, *Symp. Combust.* 12(1) (1969) 997–1005.
- [21] M.D. Smooke, I.K. Puri, K. Seshadri, A comparison between numerical calculations and experimental measurements of the structure of a counterflow diffusion flame burning diluted methane in diluted air, *Symp. Combust.* 21(1) (1988) 1783–1792.
- [22] M.D. Smoke, V. Giovangigli, Formulation of the premixed and nonpremixed test problems, *Lctr. Notes Phys.* 1991:1-28.
- [23] R.J. Kee, J.A. Miller, G.H. Evans, A computational model of the structure and extinction of strained, opposed flow, premixed methane-air flames, *Symp. Combust.* 22 (1989) 1479–1494.
- [24] A.E. Lutz, R.J. Kee, J.F. Grcar, OPPDIF: A Fortran program for computing opposed-flow diffusion flames, Sandia Report, 1997. SAND 96-8243.
- [25] F. Takahashi, V.R. Katta, A reaction kernel hypothesis for the stability limit of methane jet diffusion flames, *P. Combust. Inst.* 28(4) (2000) 2071-2078.
- [26] A.C. Zambon, H.K. Chelliah, Explicit reduced reaction models for ignition, flame propagation, and extinction of $C_2H_4/CH_4/H_2$ and air systems, *Combust. Flame* 150(1-2) (2007) 71–91.
- [27] J. Liu, X. Zhang, T. Wang, Numerical study of the chemical, thermal and diffusion

- effects of H₂ and CO addition on the laminar flame speeds of methane–air mixture, *Int. J. Hydrogen Energ.* 40 (2015) 8475–8483.
- [28] C. Yeung, M.J. Thomson, Experimental and kinetic modeling study of 1-hexanol combustion in an opposed-flow diffusion flame, *P. Combust. Inst.* 34(1) (2013) 795–802.
- [29] Guessab, Ahmed, Abdelkader, RANS Simulation of methane diffusion flame: Comparison of two chemical kinetics mechanisms, *J. Phys. Sci. Appl.* 3(6) (2013) 400-408.
- [30] R.J. Kee, G. Dixon-Lewis, J. Warnatz, A Fortran computer code package for the evaluation of gas-phase, multicomponent transport properties, Sandia Report, 1998. SAND 86-8246B.
- [31] R.J. Kee, F.M. Rupley, E. Meeks, Chemkin-III: a Fortran chemical kinetics package for the analysis of gas-phase chemical and plasma kinetics, Sandia Report, 1996. SAND-96-8216.
- [32] S. Srinivasan, J.C. Tannehill, K.J. Weilmuenster, Simplified curve fits for the thermodynamic properties of equilibrium air, NASA technical report, 1987. NASA-RP-1181.
- [33] R.A. Svehla, Estimated viscosities and thermal conductivities of gases at high temperatures, NASA technical report, 1962. NASA TR R-132.
- [34] C.Y. Wen, H.G. Hornung, Non-equilibrium dissociating flow over spheres, *J. Fluid Mech.* 299 (1995) 389-405.
- [35] K.A. Trick, T.E. Saliba, Mechanisms of the pyrolysis of phenolic resin in a carbon/phenolic composite, *Carbon.* 33(11) (1995) 1509-1515.
- [36] B. Serauskas, S. Gerg, M. Frenklach, <http://combustion.berkeley.edu/gri-mech/index.html>.